

Development and Application of an FO-LIBS System for Surrogate Nuclear Fuel

Yingge Zhang,^a Liang Tian,^{a,b} Yaju Li,^{b,d} Shuhang Gong,^{b,d} Yifan Wu,^{b,d} Xueqi Liu,^{b,d} Nasar Ahmed,^c Dongbin Qian,^{b,d,e} and Qiang Zeng^{b,d,e*}

^aSchool of Optoelectronic Science and Intelligent Instrumentation, Xi'an University of Technology, Xi'an 710048, P. R. China

^bInstitute of Modern Physics, Chinese Academy of Sciences, Lanzhou 730000, P. R. China

^cDepartment of Physics, King Abdullah Campus, The University of Azad Jammu and Kashmir, Muzaffarabad 13100, Pakistan

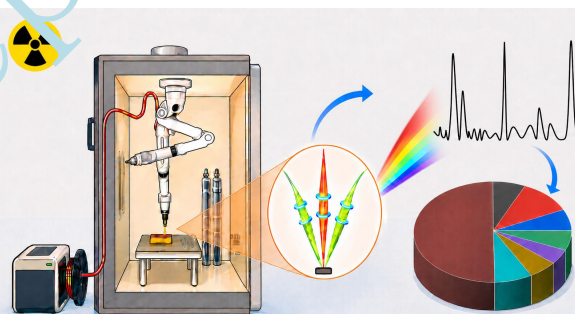
^dAdvanced Energy Science and Technology, Guangdong Laboratory, Huizhou 516000, P. R. China

^eUniversity of Chinese Academy of Sciences, Beijing 100049, P. R. China

Received: January 16, 2026; Revised: May 21, 2026; Accepted: June 02, 2026; Available online: June 02, 2026.

DOI: 10.46770/AS.2026.0002

ABSTRACT: Remote quantitative laser-induced breakdown spectroscopy (LIBS) of nuclear fuel materials is a challenging task due to unstable laser delivery and limited plasma emission collection stability. Establishing robust fiber-optic LIBS (FO-LIBS) systems with optimal operational stability is demanding. This study develops a high-throughput FO-LIBS system for quantitative analysis of CeO₂-based surrogate nuclear fuel. It incorporates a 10 m, 1 mm core multimode silica delivery fiber, a compact flat-top focusing probe, and a six-channel off-axis emission collection module with a broadband (180–900 nm) detection system. Beam profiling demonstrated that the incident Gaussian beam was transformed into a homogenized flat-top profile after fiber transmission, resulting in improved plasma stability and repeatability. Over 100 consecutive shots, the system achieved a transmission efficiency of approximately 54% with pulse energy variations of less than 2%. The full-spectrum had a relative standard deviation (RSD) of less than 5%. Internal standard normalization using Ce II emission lines produced highly linear calibration curves for La I and Nd II transitions ($R^2 > 0.99$). These findings indicate that the developed FO-LIBS system displayed stable and reproducible quantitative performance, while its detachable probe configuration provides potential flexibility for remote analysis across multiple hot cells in radiation constrained environments.



INTRODUCTION

Nuclear materials play a critical role in energy generation, fuel-cycle management, and nuclear safety.¹ Characterization of nuclear materials requires accurate and reliable elemental identification in physically and radiologically hazardous environments. Precise measurement of rare-earth elements such as lanthanum (La) and neodymium (Nd) in spent nuclear fuel (SNF) is essential for evaluating burnup and tracking fuel evolution during reactor operation.^{2,3} Although these components are crucial markers of fuel composition and history, remote measurement remains difficult. Weak emission lines, strong matrix effects, and poor spectrum repeatability under stand-off circumstances

significantly impede the quantitative detection of trace rare-earth elements in complex oxide matrices, despite that CeO₂-based surrogate fuels are commonly used to represent SNF chemistry.^{4,5} To address the challenges of nuclear material analysis under radiological restrictions, rapid, stand-off, and minimally intrusive analytical procedures are required. Laser-induced breakdown spectroscopy (LIBS) is a fast, in situ, non-destructive analytical technique that has been used for decades to detect elemental composition in solid, liquid, or gaseous materials by focusing a high power laser beam onto a sample surface to generate plasma.⁶ Qualitative analysis is achieved by identifying characteristic emission lines of the laser-induced plasma, whereas quantitative analysis is performed by correlating emission intensities with

elemental concentrations. LIBS has been widely applied in industrial applications, mineralogical research, environmental monitoring, and nuclear fuel inspection and characterization.^{7,8} In physically inaccessible environments, elemental diagnostics are critical in nuclear power plants, fuel storage pools, fuel recycling facilities, and hot cell laboratories.⁸⁻¹⁰ Limitations in direct access, the requirement to maintain safe stand-off distances to reduce radiation exposure, and restricted flexibility of optical components make standard LIBS inappropriate for such analysis.² In severe nuclear accidents, post-accident inspection requires remote, rapid, and reliable analytical techniques capable of operating in harsh environments where conventional methods are impractical.^{8, 11} These limitations emphasize the urgent need for remote, non-contact elemental analysis techniques that can provide fast, reliable compositional analysis while ensuring safety in nuclear and other high risk environments.

Recent studies have demonstrated LIBS-based chemical imaging of heterogeneous mixed-oxide samples simulating Fukushima Daiichi fuel debris, highlighting the potential of LIBS for spatially resolved characterization of complex materials relevant to nuclear applications.¹² Another work has extended LIBS to practical remote deployment through ultralong fiber-coupled microchip systems exceeding 100 m, thereby addressing standoff requirements in accident damaged or radiologically restricted facilities.^{13, 14} At the methodological level, LIBS is increasingly being combined with data-driven and multimodal strategies to improve analytical robustness. Recent examples include multi-energy spectroscopic fusion with targeted feature engineering for more accurate quantitative analysis, as well as the fusion of spectral and acoustic signals for more robust classification.^{14, 15} Also, there is a growing interest in the use of data fusion, machine learning, and quantitative modeling to improve the detection of surrogate contaminants and elemental quantification under complex conditions.^{16, 17} Taken together, these studies suggest that LIBS is moving beyond conventional single spectrum analysis toward more integrated approaches that combine instrumental development, signal enhancement, and information fusion. Among these developments, fiber-optic LIBS (FO-LIBS) is particularly attractive for nuclear applications because it enables flexible laser delivery and plasma emission collection while keeping sensitive optical and electronic components away from high radiation zones.⁴ Early engineering demonstrated long-distance, approximately 75 m, fiber-coupled FO-LIBS for in situ nuclear applications, enabling remote examination of steam generator constituents during nuclear plant shutdowns.⁹ Following the Fukushima Daiichi accident, FO-LIBS gained prominence for underwater and debris analysis, supporting successful quantitative studies on simulated nuclear fuel under submerged conditions.^{9, 11} Subsequent developments have focused on refining signal stability and analytical performance.⁷ Despite these advances, challenges related to pulse distortion and limited spectral repeatability emphasize the need for optimization of FO-

LIBS systems.^{11, 18} Long-pulse laser excitation and microwave-assisted LIBS have also demonstrated enhanced plasma stability, emission intensity, and improved signal-to-noise ratio^{19, 20}. In addition, to address matrix effects and signal instability in complex materials, sophisticated data processing and chemometric techniques, including multivariate statistical and machine-learning based methodologies, have been used. The necessity for integrated FO-LIBS systems is highlighted by the fact that although these methods provide significant performance gains, they are mainly application specific and do not directly resolve fundamental issues of laser delivery stability and photon collection efficiency.^{3, 9} Despite considerable advancements in FO-LIBS, most studies have primarily focused on sensitivity enhancement and data processing, while engineering-grade system stability, laser delivery robustness, and spectral repeatability remain insufficiently addressed.^{21, 22} Long-distance laser delivery stability, optical throughput, and shot-to-shot repeatability are critical elements controlling quantitative reliability in practical applications.² Instabilities in laser transmission and ineffective photon collection directly cause variations in ablation conditions, increased relative standard deviation, and reduced confidence in elemental quantification. Reproducibility and robustness are therefore more important for nuclear safety, material accountability and post-accident evaluation than peak sensitivity achieved under ideal laboratory conditions. This finding underscores a significant gap in current FO-LIBS research and encourages system designs that prioritize stable operation over sensitivity.²³ In the present work, a high-throughput, long-distance FO-LIBS system optimized for stable operation is developed to satisfy engineering requirements in radiation relevant environments. The system incorporates a 10 m, 1 mm-core, large-aperture silica delivery fiber with a coupling interface for robust transmission of high energy nanosecond pulses with minimal fluctuation. The probe features a compact conical front end with integrated focusing optics and a six-channel off-axis emission collection assembly, improving photon capture efficiency without beam splitting optics. Coupled to a spectrometer array covering 180–900 nm, the system enables broadband, high-throughput detection with enhanced repeatability. Demonstrated on CeO₂-based surrogate spent fuel doped with rare-earth oxides, the system exhibits stable laser transmission, low pulse-to-pulse RSD, and high spectral reproducibility. Calibration results for key rare-earth transitions show excellent linearity ($R^2 \approx 0.99$), confirming the system's capability for remote, robust nuclear material inspection.

In contrast to previous FO-LIBS studies that primarily emphasize long-distance deployment or sensitivity enhancement, the present work focuses on system level integration to achieve improved laser delivery stability, spectral repeatability, and quantitative robustness under practical operating conditions. Earlier studies have demonstrated the feasibility of long-distance fiber-coupled deployment for nuclear applications. However, the

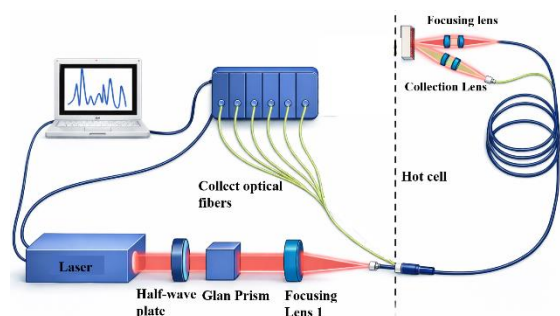


Fig. 1 Optical layout of the developed FO-LIBS system.

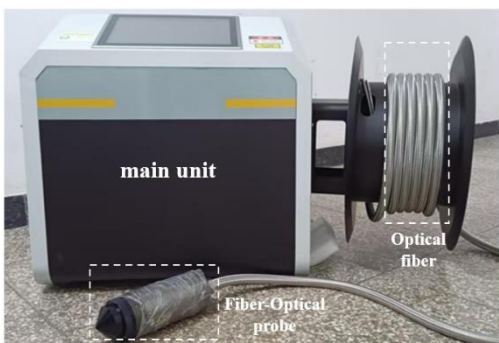


Fig. 2 Photograph of the assembled FO-LIBS system.



Fig. 3 (a) Schematic of the hot cell deployment configuration;(b) Conceptual deployment of the detachable FO-LIBS system for hot cells group applications.

integration of stable high energy fiber delivery, compact probe-side plasma collection, broadband synchronized detection, and a detachable probe configuration for deployment in multiple hot cells remains insufficiently explored in FO-LIBS systems designed for nuclear relevant environments. In the present work, the system delivered up to 48 mJ at the fiber output after 10 m transmission through a 1 mm-core multimode silica fiber, with an average transmission efficiency of approximately 54% and pulse-to-pulse fluctuations below 2% root-mean-square (RMS). The focusing optics produced a focal spot of approximately 500 μm , and after fiber delivery the average full-spectrum RSD decreased from 5.97% to 4.15%, indicating improved spectral repeatability under the present operating conditions. Therefore, the main contribution of the present study lies not in remote deployment or multi-channel collection alone, but in combining stable high energy fiber delivery, compact probe-side plasma collection, and broadband synchronized detection into a unified FO-LIBS

platform with improved transmission stability, spectral repeatability, and quantitative robustness.

CONFIGURATIONS AND MATERIALS

System configuration. Figure 1 shows a schematic representation of the optical layout of the developed FO-LIBS system. The Nd:YAG laser was used as the excitation source and coupled into a large-core multimode fiber through a beam conditioning and coupling assembly. The laser pulse was then transmitted through the delivery fiber to a miniature fiber-optic probe, where it was focused onto the sample surface to generate plasma. Six off-axis channels embedded within the probe collected the plasma optical emission, which was subsequently guided via optical fibers to a multi-spectrometer array for spectral identification. Fig. 2 shows a photograph of the implemented system, including the laser delivery unit, the fiber-optic probe, and the multi-spectrometer detection module. Fig. 3a illustrates a representative single hot cell deployment scenario, in which the laser source and spectrometers are positioned outside the shielded area, while the probe head is inserted into the cell for remote analysis. Fig. 3b further illustrates the potential deployment of the system for multiple hot cells. In this configuration, each hot cell is equipped with an independent probe interface, and the detachable fiber connector allows the external main unit to be coupled to the interface of each hot cell when needed. The system consists of three major functional modules: a laser delivery unit for beam homogenization and fiber coupling, a fiber-optic probe with focusing and off-axis multi-channel collection, and a spectrometer array for synchronized broadband detection. All optical and mechanical components were mounted on precision adjustable supports to ensure stable energy transmission and consistent spectral performance. The 10 m delivery fiber was selected based on the intended application, where a moderate routing distance is required between the main unit and the interface.

The excitation source was a Q-switched Nd:YAG laser (DAWA-300, Beamtech Optronics Co., China) operating at a wavelength of 1064 nm, with a pulse width of 7 ns, and a maximum pulse energy of 300 mJ. The beam initially passed through a half-wave plate and a Glan prism, which together functioned as an adjustable attenuator. This design enabled precise control over the delivered energy while maintaining stable laser operation. The attenuated beam was then coupled into a 10 m long, 1 mm-core silica multimode fiber ($\text{NA} \approx 0.22$) through a Quartz Block Head (QBH)-compatible industrial grade connector assembly. The coupling optics employed a lens group with an equivalent focal length of 50 mm. The beam diameter at the fiber input facet was adjusted to approximately 90% of the fiber core diameter, and the incident beam had an NA of approximately 0.20, which remained within the fiber acceptance NA. A 2D micro-

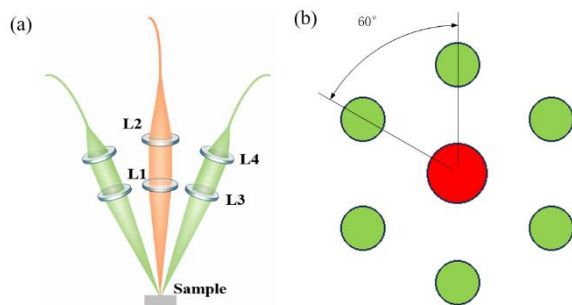


Fig. 4 Schematic illustration of the FO-LIBS probe. (a) Side view showing the longitudinal optical configuration. L1–L2: focusing and collimating lenses for laser delivery; (b) Top view showing the complete six-channel circular arrangement around the central focusing channel. L3–L4: off-axis collection lenses that direct plasma emission to the spectrometer array.

positioning stage was used to optimize the coupling alignment. The fiber end face was prepared by mechanical polishing followed by laser preconditioning before high energy operation.

Figure 4 shows the optical configuration of the FO-LIBS probe with stable laser delivery achieved. Six collection channels are distributed circumferentially around the central excitation/focusing channel. In the side-view schematic, only two representative collection channels are shown for clarity, while the complete six-channel arrangement is provided in the top-view figure. This probe was designed to ensure reproducibility of emission spectra and improve photon collection under remote operating conditions. A pair of lenses (L1–L2) was used to focus the laser beam onto the sample. Plasma emission was collected from six symmetrically organized off-axis channels, each equipped with a two-lens collection system (L3–L4). This off-axis configuration was preferred because it improved photon collection efficiency and spectral consistency. A key innovation of the developed system lies in the design of a compact conical fiber-optic probe that integrates focusing optic and multi-channel off-axis collection within a single sealed housing. To protect the optical components during experiments in contaminated or radiation rich environments, a lead-glass protective window was mounted on the probe front. This window acted as shielding against dust, debris, or radioactive particulates.

The focusing assembly of the FO-LIBS probe was first designed and evaluated using Zemax OpticStudio to ensure that the delivered laser energy could be efficiently and stably concentrated onto the sample surface. A pair of fused-silica plano-convex lenses ($f = 75$ mm) was used as the collimating and focusing elements due to their high damage threshold and low chromatic dispersion at the operational wavelength. Ray tracing simulations were performed to optimize the spacing between the two lenses, minimize spherical aberration, and achieve a stable focal spot within the required working distance. The light spot was approximately $500 \mu\text{m}$ at the focal plane, this focal diameter was

deemed suitable for generating stable plasma while avoiding excessive local fluence within the multimode fiber. The simulation further predicted that the beam intensity at the focal region would retain a relatively uniform, flat-top profile due to the modal scrambling inherent to the large-core fiber and the low aberration lens configuration. This homogenized distribution is advantageous for producing repeatable ablation behavior and mitigating shot-to-shot variations in plasma initiation.

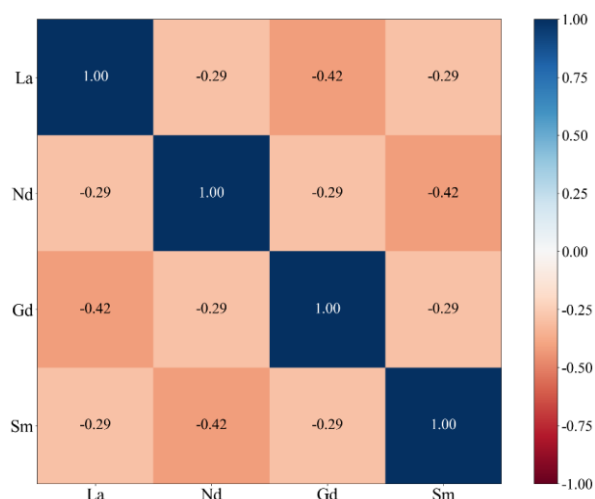
Plasma emission was collected through six symmetrically arranged off-axis optical channels, each positioned at approximately 21° relative to the laser axis. Each channel consisted of two 0.5-inch fused-silica lenses ($f = 35$ mm) that focused the collected emission into an individual optical fiber. This off-axis multi-channel configuration eliminates the need for beam splitting optics typically required in coaxial collection schemes, thereby reducing optical loss. The six independent collection fibers enable simultaneous acquisition of plasma emission from multiple viewing angles, providing spatially averaged spectral information. All collection channels were integrated into a rigid concentric mechanical frame, ensuring fixed geometry, mechanical stability, and ease of alignment during probe assembly and operation.

The optical emission collected by the six fibers integrated in the probe was recorded by a synchronized six-channel spectrometer system (AvaSpec Multi-Channel Spectrometer, The Netherlands). The six collection channels were connected to the same spectrometer platform, equipped with 4096-pixel CMOS detector arrays with a pixel size of $14 \times 200 \mu\text{m}$. Each channel employed the same hardware configuration, including a UF grating of 3600 lines mm^{-1} , a $10 \mu\text{m}$ entrance slit, a DCL-200 detector sensitivity enhancement module, and an OSF-CAF purge lens assembly. The six channels differed only in their wavelength settings and together covered the spectral range from 180 to 900 nm: CH1, 180–253 nm; CH2, 252–314 nm; CH3, 312–416 nm; CH4, 414–498 nm; CH5, 496–700 nm; and CH6, 698–900 nm. The spectral resolution was 0.06–0.08 nm. The spectrometer system was externally triggered by the laser Q-switch signal, and the synchronized acquisition of the six spectral channels was managed by the internal timing logic of the multi-channel spectrometer system. The spectra were automatically merged in AvaSoft to reconstruct a broadband spectrum over the full 180–900 nm range. For data analysis, the acquired spectra were exported and further processed in Python, including background subtraction, spectral averaging and internal standard correction. To minimize spectral interference, relatively isolated lines were preferentially selected, especially for those located away from channel boundaries and major neighboring Ce/REE emissions.

Sample preparation and experimental procedures. To evaluate the quantitative performance of the developed FO-LIBS system under controlled and reproducible conditions, surrogate spent-fuel samples were prepared using CeO_2 as the matrix, doped with

Table 1. Elemental composition (wt%) of the sample

Sample	La(%)	Nd(%)	Gd(%)	Sm(%)	Ce(%)
1	0.50	4.26	4.5	0.75	89.99
2	0.75	0.51	4.25	4.51	89.98
3	1.02	2.76	1.26	5.02	89.94
4	1.26	5.04	1.01	2.77	89.92
5	1.51	2.01	3.02	3.51	89.95
6	2.02	3.02	3.51	1.50	89.95
7	2.75	1.29	5.06	1.03	89.92
8	4.28	4.50	0.76	0.51	89.95
9	4.50	0.75	0.50	4.25	90.00

**Fig. 5** Pearson correlation matrix of mass fractions of La, Nd, Sm, Gd, and Ce in surrogate nuclear fuel samples.

La₂O₃, Nd₂O₃, Sm₂O₃, and Gd₂O₃ to construct a multi-element rare-earth oxide system. Nine groups of samples with different elemental concentration combinations were fabricated, as summarized in Table 1. The preparation involved weighing the oxide powders according to the target mass ratios them in deionized water, followed by mechanical stirring for 15 min to ensure homogeneity. The slurry was vacuum filtered to remove excess water and subsequently dried in a muffle furnace at 1000 °C for 4 h. The dried powders were ground and pressed into pellets with a diameter of 2 cm, a thickness of ~3 mm, and a mass of approximately 4 g using a uniaxial pressing force of 2 tons for 2 min. The resulting pellets exhibited good mechanical stability and surface uniformity. To verify the statistical independence of elemental distributions in the prepared surrogate fuel samples, Pearson correlation analysis was performed on the mass fractions of La, Nd, Sm, Gd, and Ce. As shown in Fig. 5, the correlation coefficients ranged from 0.29 to 0.42, indicating no significant linear dependence among the elements. This finding confirms that the prepared multi-element samples exhibit minimal compositional coupling, which is essential for reliable quantitative modeling.

During FO-LIBS measurements, the laser energy at the fiber output was fixed at 42 mJ. The sample pellet was translated by a

motorized XYZ stage in a matrix-scanning pattern at a speed of 1 mm s⁻¹ under a laser repetition rate of 1 Hz, corresponding to an inter-pulse displacement of 1 mm. This ensured that each pulse irradiated a fresh surface location and minimized cumulative single spot ablation effects. The acquisition delay and integration time used for quantitative measurements were set to 1.5 μs and 10 μs, respectively. For each sample, 100 single shot spectra were acquired, and all spectra were retained for subsequent analysis. The 100 spectra were then averaged to obtain a representative spectrum for internal standard normalization and quantitative calibration.

In addition, to evaluate the effect of fiber coupling on plasma temperature fluctuations, measurements were carried out using an alloy steel sample under identical experimental conditions before and after fiber coupling. The laser pulse energy was fixed at 42mJ for both measurements. The detection delay and gate width were set to 0.5 μs and 10 μs, respectively, and 100 spectra were recorded for each condition.

RESULTS AND DISCUSSION

In this section the experimental results obtained using the developed FO-LIBS system are presented, with emphasis on linking system design choices to plasma behavior, spectral stability, and quantitative performance. The findings are organized to demonstrate; the transformation of the excitation beam profile, the resulting laser transmission efficiency and spectral repeatability, and the implications of these properties for quantitative analysis in complex rare-earth oxide matrices.

Beam profile and plasma stability. Following the system design and optical configuration described, the spatial characteristics of the excitation beam were experimentally examined to validate the optical design and to assess the impact of fiber delivery on laser plasma interaction. To further validate and contextualize the Zemax simulation, the beam profile was independently characterized before entering the fiber and after exiting the fiber. Prior to fiber injection, a beam quality analyzer was used to characterize the laser focal spot. Fig. 6(a) shows the focal spot of the laser prior to fiber coupling, measured using a laser beam quality analyzer, where the incident beam exhibited a near-Gaussian intensity distribution. The focusing spot in Fig. 6(b) had a diameter of approximately 600 μm, consistent with the simulated value of ~500 μm when considering alignment tolerances and the mode-dependent divergence inherent to multimode fiber propagation. Notably, the post-fiber beam exhibited a distinct flat-top (top-hat) intensity distribution, in contrast to the near-Gaussian profile observed prior to fiber injection.

This transformation is attributed to pulse broadening and modal dispersion occurring during high energy transmission through the

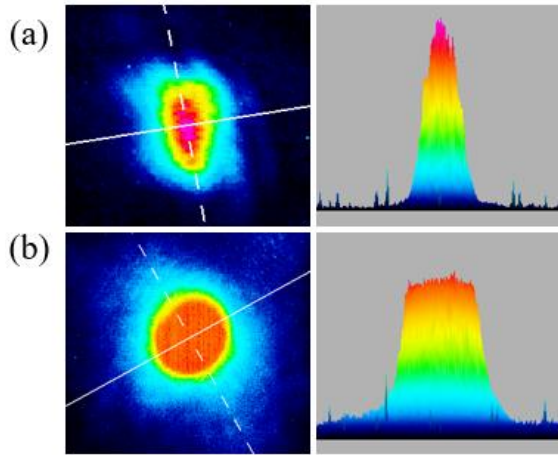


Fig. 6 Beam-quality measurements obtained with the beam profiler. (a) Spatial beam distribution prior to fiber coupling; (b) spatial beam distribution following transmission through the fiber.

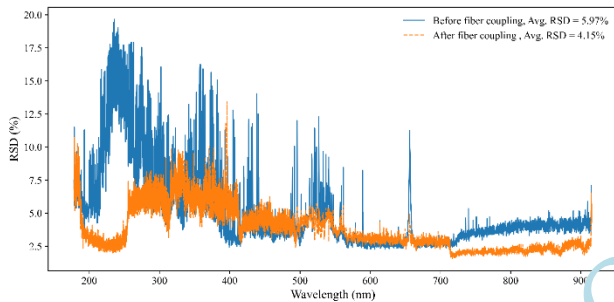


Fig. 7 Full-spectrum RSD comparison before and after fiber coupling.

large-core multimode fiber.^{24, 25} Such modification in the spatial energy distribution directly affects plasma formation, motivating a closer examination of the factors governing emission intensity. Under local thermodynamic equilibrium, the emission line intensity I_k follows the Boltzmann distribution:

$$I_k = F C_s \frac{A_k g_k}{U^z(T)} e^{-\left(\frac{E_k}{k_B T}\right)} \quad (1)$$

where F factor is related to the ablated mass, I_k indicates the line intensity, C_s denotes the concentration of neutral atoms, A_k refers to the transition probability, g_k represents the statistical weight of the upper level, $U^z(T)$ corresponds to the partition function, E_k implies the energy of the upper level, k_B denotes the Boltzmann constant, and T is the plasma excitation temperature. According to Eq. (1), the emission line intensity is primarily governed by plasma temperature. Therefore, to investigate how fiber delivery affects plasma excitation, the apparent excitation temperature was estimated before and after fiber coupling using the same alloy steel sample. The estimation was performed using the Boltzmann plot method based on selected Fe atomic emission lines (Table S1).

For the directly focused Gaussian beam, the high peak intensity and strong spatial gradients may promote localized energy deposition and plasma shielding at the laser-plasma interface, resulting in less stable plasma excitation. In contrast, after fiber coupling, the beam profile tends to become more spatially homogenized, which can suppress local hot-spot formation and promote more uniform energy deposition on the sample surface. Based on the Boltzmann plot estimation (Fig. S1), the average apparent excitation temperatures before and after fiber coupling were approximately 11789 K and 8781 K, respectively (Fig. S2). More importantly, the RSD of the estimated apparent excitation temperature decreased from 2.84% before fiber coupling to 1.26% after fiber coupling (Fig. S2), suggesting a more reproducible excitation condition after fiber transmission.

To evaluate the shot-to-shot spectral stability before and after fiber coupling, the RSD of the spectral intensity was calculated over the full wavelength range. For each wavelength λ , the RSD was defined as

$$RSD(\lambda) = \frac{\sqrt{\frac{1}{N-1} \sum_{i=1}^N [I_i(\lambda) - \bar{I}(\lambda)]^2}}{\bar{I}(\lambda)} \times 100\% \quad (2)$$

where $I_i(\lambda)$ is the spectral intensity at wavelength λ for the i -th shot, $\bar{I}(\lambda)$ is the mean intensity at that wavelength over N repeated measurements, and N is the total number of spectra. The average full-spectrum RSD was then calculated as

$$R\bar{S}D = \frac{1}{M} \sum_{j=1}^M RSD(\lambda_j) \quad (3)$$

where M is the total number of wavelengths.

Figure 7 shows the wavelength resolved RSD profiles before and after fiber coupling. Compared with the directly focused beam, the fiber-coupled beam exhibits lower RSD values over a broad spectral range, indicating improved shot-to-shot repeatability of the emission signal. Quantitatively, the average full-spectrum RSD decreased from 5.97% before fiber coupling to 4.15% after fiber coupling. This result provides more direct evidence that fiber coupling improves the stability of spectral emission. Together with the reduced dispersion of the Boltzmann estimated apparent excitation temperature, these results suggest that fiber delivery leads to a more reproducible plasma excitation process.

Laser transmission and pulse stability. The output energies were recorded over a range of incident energies from 8 mJ to 48 mJ. As shown in Fig. 8, the overall transmission efficiency remained stable at an average of approximately 54%, with pulse-to-pulse RMS fluctuations below 2%. It should be noted that this 54% value represents the overall system transmission efficiency, defined as the ratio of the fiber-output pulse energy to the pulse energy measured immediately before coupling. Therefore, it includes not only the coupling loss at the fiber input, but also the propagation and interface losses of the complete fiber delivery

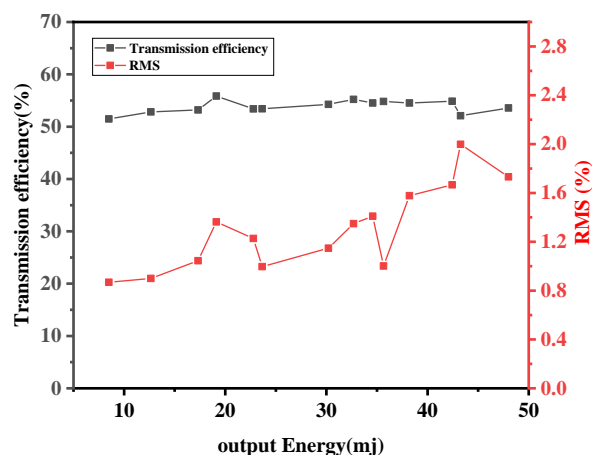


Fig. 8 Input-output energy relationship and transmission stability of the FO-LIBS system.

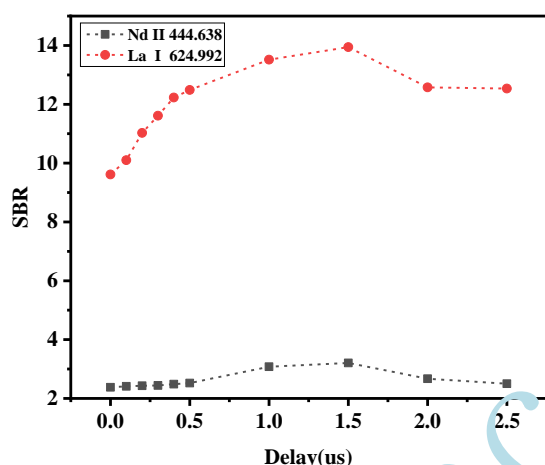


Fig. 9 Variation of SBR with acquisition delay time for representative emission lines (La I at 624.992 nm and Nd II at 444.638 nm).

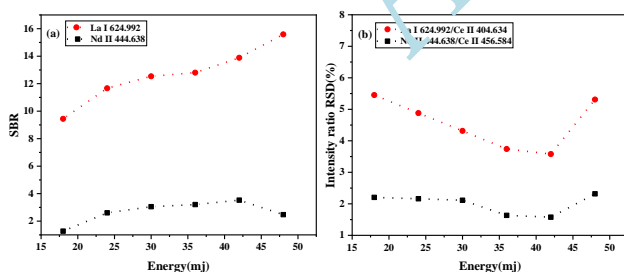


Fig. 10 (a) Signal-to-background ratio of La I 624.992 nm and Nd II 444.638 nm at different pulse energies. (b) RSD of internal standard line ratios at different pulse energies.

system, rather than the coupling efficiency alone. These results demonstrate that the coupling interface, combined with the large-core silica fiber, enables stable and efficient delivery of high energy nanosecond pulses over a 10 m distance. The equivalent average fluence and irradiance at the maximum stable output

energy were estimated to be approximately 7.6 J/cm² and 1.1 GW/cm², respectively. These estimated values are below the bulk damage threshold irradiance reported for fused silica at 1064 nm²⁶, providing a reasonable material-level safety margin for the present operating condition.

Optimization of Experimental Conditions. The experimental parameters were further optimized to maximize analytical performance, based on the FO-LIBS system's intrinsic transmission stability and plasma emission reproducibility described in Section 3.2. In LIBS, the excitation laser energy and the spectral acquisition delay time are two critical parameters that influence plasma growth and the resulting signal-to-background ratio (SBR).²⁷ In this study, the SBR was determined by extracting the peak intensity within a narrow spectral window centered on the emission line of interest. The background level was estimated from two flanking regions located on either side of the line, at distances ranging from one to two times the selected background width parameter. The average intensity of these adjacent regions was used to represent the baseline. The SBR was then defined as the ratio of the peak signal intensity to the mean background level.

In this study, delay times were scanned from 0.5 μ s to 2.5 μ s using the La I 624.992 nm and Nd II 444.638 nm lines as representative analytes. At shorter delays (<1 μ s), the emission lines exhibited high absolute intensities; however, strong continuum radiation resulted in reduced SBR values. At longer delays (> 2 μ s), the background diminished substantially, but the analyte signals also decayed, again leading to lower SBR. The optimal range was identified between 1 and 2 μ s, with the best overall performance at approximately 1.5 μ s. Notably, as shown in Fig. 9, the overall SBR of La I 624.992 nm was consistently lower than that of the Ce II internal standard lines, which may be attributed to the sample selected for parameter testing (Sample 1), where the La concentration was the lowest and Nd concentration relatively higher. Nevertheless, the La and Nd lines maintained SBR values greater than 3 at 1.5 μ s, confirming their suitability for reliable peak identification. Based on these results, an acquisition delay of 1.5 μ s was selected for all subsequent quantitative analyses.

After the acquisition delay had been fixed at 1.5 μ s, the effect of output pulse energy on analytical performance was further investigated to justify the energy used in subsequent quantitative measurements. Here, the quoted pulse energies refer to the laser energy measured at the fiber output. Spectra were recorded at different output pulse energies and the SBR was evaluated using the same representative analytical lines, La I 624.992 nm and Nd II 444.638 nm. The maximum energy was limited to 48 mJ in consideration of the transmission threshold of the delivery fiber, so as to avoid operating too close to the fiber damage threshold. As shown in Fig. 10a, the SBR of La I 624.992 nm generally decreased with decreasing pulse energy, whereas the SBR of Nd II 444.638 nm

Table 2. Selected analytical lines and internal standards

Wavelength(nm)	Source	$E_j(\text{cm}^{-1})$	Nearby interference	Reason for selection
La I 624.992	NIST ASD	20117.38	No interference	Strong analyte response, acceptable SBR, and limited overlap with adjacent lines in the CeO ₂ -based matrix
Ce II 404.634	NIST ASD	29166.597	NdII 404.080 La II 404.291 Gd II 404.684	Stable and intense matrix line; used to compensate for shot-to-shot fluctuation in plasma conditions
Nd II 444.638	NIST ASD	24134.08	Ce II 444.439	Representative Nd line with usable SBR and limited spectral interference
Ce II 456.584	NIST ASD	30669.702	La II 455.846	Stable matrix emission with good intensity and minimal overlap in the selected spectral window
Gd I 419.078	NIST ASD	24854.297	Nd II 417.732 Gd II 418.425 La II 419.655	It showed a clear and detectable emission signal with limited overlap from adjacent lines in the inspected spectral region.
Ce II 418.732	NIST ASD	28334.756	Nd II 417.732 Gd II 418.425 Gd I 419.078	This line exhibited stable and sufficiently intense emission across all samples.
Sm I 484.17	NIST ASD	24668.79	Ce I 484.777	It provided a favorable signal response with limited overlap from neighboring emissions.
Ce II 452.308	NIST ASD	26268.203	La II 452.237 La II 452.612 Ce II 452.73	It showed stable and intense matrix emission and was suitable for normalizing the neighboring analyte.

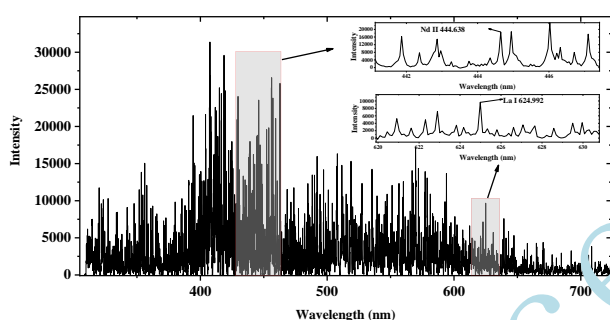


Fig. 11 Broadband LIBS spectra using a 1064 nm Nd:YAG laser (7 ns pulse width, 42 mJ pulse energy, 1 Hz repetition rate), with a 1.5 μs detection delay and 10 μs gate width of rare-earth-doped CeO₂. Inset's depict the analyte emission lines selected for quantitative analysis.

first increased and then decreased, reaching its maximum at 42 mJ.

In addition to the SBR analysis, the repeatability of the internal standard line ratios was further evaluated at different pulse energies using the RSD of La I 624.992/Ce II 404.634 and Nd II 444.638/Ce II 456.584. As shown in Fig. 10b, both line-ratio RSDs decreased from 18 to 42 mJ and increased again at 48 mJ. The minimum RSD values were obtained at 42 mJ, reaching 3.58% for La I 624.992/Ce II 404.634 and 1.58% for Nd II 444.638/Ce II 456.584. Considering both sensitivity and quantitative repeatability, 42 mJ was selected as the best overall compromise energy for subsequent measurements. The influence of gate width on the spectral profile and SBR was relatively limited, so the gate width was fixed at 10 μs throughout the study to obtain relatively strong emissions.

Calibrations. Figure 11 shows representative spectra acquired from the rare-earth-doped CeO₂ samples, all the spectra were

acquired under identical experimental conditions. Considering the spectral complexity of the rare-earth-doped CeO₂ matrix, polynomial baseline fitting was applied to each single-shot spectrum for background correction. After background subtraction, the spectra were averaged and subjected to internal standard normalization. The confirmed emission peaks were assigned with reference to the NIST Atomic Spectra Database, using a wavelength matching tolerance of ± 0.08 nm. The selected analytical lines and internal standard lines, together with their database sources, nearby interference candidates, and selection rationale, are summarized in Table 2.

Under these conditions, calibration based solely on the raw emission intensities of the analyte lines showed poor linearity and limited quantitative reliability, mainly because of matrix effects and fluctuations in plasma conditions. To mitigate these effects, an internal standard normalization strategy was adopted, as defined in Eq. (4):

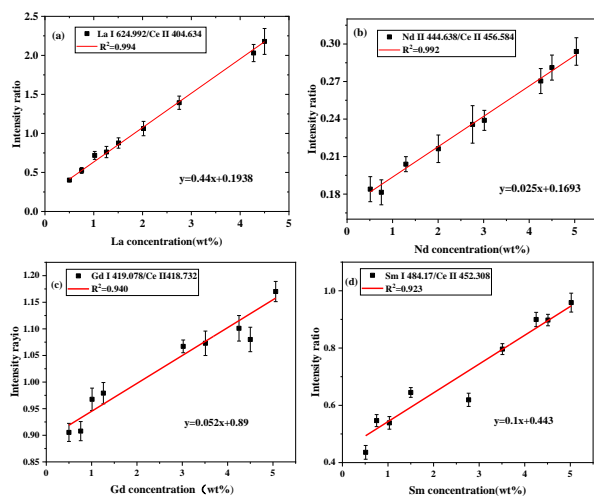
$$N_{\text{element}}^i = \frac{I_{\text{element}}^i}{I_{\text{Ce}}^i} \quad (i = 1, 2, 3, \dots, n) \quad (4)$$

where I_{element}^i is the intensity of the analytical line of the target element, and I_{Ce}^i is the intensity of the corresponding Ce internal standard line. Ce lines were chosen as internal standards because Ce is the dominant matrix element. Each analyte line was normalized to the corresponding Ce line to reduce shot-to-shot variations associated with plasma temperature, electron density, and ablation fluctuations.

Based on the signal-to-background ratio and local spectral interference analysis, four analytical line pairs were selected for quantitative evaluation. Fig. 12 presents the normalized calibration curves, and the corresponding calibration metrics are summarized in Table 3, including the coefficient of determination (R^2) before

Table 3. Calibration parameters of the selected line pairs

Characteristic spectral lines	R ² (raw)	Characteristic spectral lines	R ² (normalized)	Slope±Confidence Interval	RMSE	LOD
La I 624.992	0.960	Ce II 404.634	0.994	0.439±0.0190	0.028	0.047%
Nd II 444.638	0.870	Ce II 456.584	0.992	0.024±0.0017	0.003	0.12%
Gd I 419.078	0.800	Ce II 418.732	0.940	0.052±0.0116	0.022	0.35%
Sm I 484.17	0.904	Ce II 452.308	0.923	0.104±0.0240	0.044	0.20%

**Fig. 12** Internal standard normalized calibration curves obtained with the FO-LIBS system: (a) La I 624.992 nm normalized to Ce II 404.634 nm; (b) Nd II 444.638 nm normalized to Ce II 456.584 nm; (c) Gd I 419.078 nm normalized to Ce II 418.732 nm; (d) Sm I 484.17 nm normalized to Ce II 452.308 nm.

and after internal standard normalization, slope with confidence interval, Root Mean Square Error (RMSE), and limit of detection (LOD). The LOD was estimated from the calibration slope and the standard deviation of repeated measurements according to

$$LOD = \frac{3\sigma}{k} \quad (5)$$

where σ is the standard deviation of the reference spectra used for LOD estimation, and k is the slope of the corresponding calibration curve.

Among the four rare-earth elements investigated, La and Nd exhibited the best quantitative performance, with R^2 values of 0.994 and 0.992, respectively, together with relatively low RMSE and LOD values. By contrast, the calibration results for Gd and Sm were less satisfactory, with R^2 values of 0.940 and 0.923, respectively, and noticeably higher RMSE and LOD values. The poorer quantitative performance of Gd and Sm is mainly attributed to the more congested spectral regions surrounding the selected lines and the stronger influence of nearby interfering emissions, as indicated in Table 3. In addition, the complex CeO₂ matrix background increases the uncertainty of peak extraction and internal standard normalization for these two elements. Overall, the developed FO-LIBS system demonstrates multi-element detection capability in the CeO₂-based surrogate fuel matrix, La and Nd remain the most reliable analytical channels under the

present spectral resolution and line selection conditions. For more complex matrices or real nuclear fuels, more elaborate experimental design would be combined with advanced data processing approaches in the future.

CONCLUSION

A reliable long-distance FO-LIBS system was designed and quantitatively validated using CeO₂ as a surrogate matrix. Laser delivery through a 10 m large-core multimode silica fiber, paired with a compact probe incorporating flat-top beam focusing and six-channel off-axis plasma emission collection, resulted in improved excitation uniformity and photon throughput. Multimode fiber delivery successfully converted the Gaussian beam into a homogenized intensity profile, leading to stable plasma generation with low pulse-to-pulse energy fluctuations, high transmission efficiency, and reduced spectral variability. After optimization of acquisition parameters, quantitative analysis in a spectrally congested rare-earth oxide matrix demonstrated excellent linearity and repeatability using internal standard normalization. In addition, the detachable probe configuration provides potential flexibility for deployment across multiple hot cells. These findings confirm that beam homogenization, transmission stability, multi-channel emission collection, and detachable probe integration are essential for robust quantitative FO-LIBS, enabling its application in remote elemental diagnostics within radiation constrained and inaccessible environments.

ASSOCIATED CONTENT

The data supporting this article (Tables S1 and Figs. S1-S2) is available at <https://www.at-spectrosc.com>

AUTHOR INFORMATION

XXX

Corresponding Author

* Q. Zeng

Email address: zeng.qiang@impcas.ac.cn

Notes

The authors declare no competing financial interest.

ACKNOWLEDGMENTS

The authors gratefully thank the National Natural Science Foundation of China (U2241288, 11974359 and 52405600) for financial support of this work.

REFERENCES

1. N. Todreas and M. Kazimi, *Nuclear Systems Volume I: Thermal Hydraulic Fundamentals*. Boca Raton, CRC Press, 2021.
2. K. Tamura, H. Ohba, M. Saeki, T. Taguchi, H. H. Lim, T. Taira, and I. Wakaida, *J. Nucl. Sci. Technol.*, 2020, **57**, 1189-1198. <https://doi.org/10.1080/00223131.2020.1776648>
3. M. Salvatores and G. Palmiotti, *Prog. Part. Nucl. Phys.*, 2011, **66**, 144-166. <https://doi.org/10.1016/j.pnpnp.2010.10.001>
4. M. Saeki, A. Iwanade, C. Ito, I. Wakaida, B. Thornton, T. Sakka, and H. Ohba, *J. Nucl. Sci. Technol.*, 2014, **51**, 930-938. <https://doi.org/10.1080/00223131.2014.917996>
5. A. W. Miziolek, V. Palleschi, and I. Schechter, *Laser Induced Breakdown Spectroscopy*. Cambridge, Cambridge University Press, 2006.
6. L. J. R. David A. Cremers, in *Handbook of Laser-Induced Breakdown Spectroscopy*. 2013, pp 257-287.
7. S. Shahida, N. Ahmed, S. Razzaque, A. Jabbar, M. Rafique, M. I. Khan, M. Hafeez, and M. A. Baig, *Laser Phys.*, 2021, **31**, 105601. <https://doi.org/10.1088/1555-6611/ac2b96>
8. C. Ito, H. Naito, A. Nishimura, H. Ohba, I. Wakaida, A. Saegiyama, and K. Chatani, *J. Nucl. Sci. Technol.*, 2014, **51**, 944-950. <https://doi.org/10.1080/00223131.2014.924883>
9. A. I. Whitehouse, J. Young, I. M. Bohe, and S. Lawson, C. P. Evans, and J. Wright, *Spectrochim. Acta B*, 2011, **56**, 821-830. [https://doi.org/10.1016/S0584-8547\(01\)0232-4](https://doi.org/10.1016/S0584-8547(01)0232-4)
10. A. K. Rai, F. Y. Yueh, J. P. Singh, and H. Zhang, *Rev. Sci. Instrum.*, 2002, **73**, 3589-3599. <https://doi.org/10.1063/1.1505101>
11. M. Zhang, H. Fu, H. Wang, B. Wu, Y. Liu, and Z. Zhang, *Spectrochim. Acta B*, 2023, **210**, 106818. <https://doi.org/10.1016/j.sab.2023.106818>
12. S. Almaviva, T. Karino, K. Akaoka, and I. Wakaida, *Spectrochim. Acta B*, 2024, **218**, 106960. <https://doi.org/10.1016/j.sab.2024.106960>
13. M. Batsaikhan, H. Ohba, and I. Wakaida, *Optics Express*, 2024, **32**, 45158. <https://doi.org/10.1364/oe.541447>
14. W. Gao, B. Han, Z. Sun, Y. Zhang, and Y. Liu, *Anal. Chem.*, 2026, **98**, 7489-7502. <https://doi.org/10.1021/acs.analchem.5c06997>
15. S. Liu, Y. Zhang, J. Feng, W. Gao, T. Li, and Y. Liu, *Opt. Lett.*, 2026, **51**, 949-952. <https://doi.org/10.1364/OL.576900>
16. J. I. Braun, P. E. Anderson, J. I. Borrero Negrón, K. C. Hartig, and A. P. Rao, *Appl. Spectrosc.*, 2025, **79**, 1078-1090. <https://doi.org/10.1177/00037028241298305>
17. S. Kumar, S. Maji, and K. Sundararajan, *J. Radioanal. Nucl. Ch.*, 2025, **334**, 4225-4232. <https://doi.org/10.1007/s10967-024-09763-5>
18. M. Tampo, M. Miyabe, K. Akaoka, M. Oba, H. Ohba, Y. Maruyama, and I. Wakaida, *J. Anal. Atom. Spectrom.*, 2014, **29**, 886-892. <http://dx.doi.org/10.1039/C3JA50259G>
19. W. Gu, Z. Hou, W. Song, L. Li, X. Yu, J. Liu, Y. Song, M. S. Afgan, Z. Li, Z. Liu, and Z. Wang, *Anal. Chim. Acta*, 2022, **1205**, 339752. <https://doi.org/10.1016/j.aca.2022.339752>
20. L. Brunnbauer, Z. Najarska, T. Lohninger, and A. Limbeck, *TrAC-Trends Anal. Chem.*, 2023, **159**, 116859. <https://doi.org/10.1016/j.trac.2022.116859>
21. R. Noll, *Laser-Induced Breakdown Spectroscopy: Fundamentals and Applications*. Heidelberg, Springer Berlin, 2012.
22. R. Noll, C. Fricke-Begemann, M. Brunk, S. Connemann, C. Meinnardt, M. Scharun, V. Sturm, J. Makowe, and C. Gehlen, *Spectrochim. Acta B*, 2014, **93**, 41-51. <https://doi.org/10.1016/j.sab.2014.02.001>
23. A. Sarkar, R. K. Mishra, C. P. Kaushik, P. K. Watal, D. Alamelu, and S. K. Aggarwal, *Radiochim. Acta*, 2014, **102**, 805-812. <https://doi.org/10.1515/ract-2014-2243>
24. Y. Qiu, J. Wu, Z. Zhang, T. Liu, F. Xue, Y. Hang, Y. Wu, H. Yu, and X. Li, *Spectrochim. Acta B*, 2019, **155**, 12-23. <https://doi.org/10.1016/j.sab.2019.03.003>
25. X. Xiao, S. Le Berre, D. G. Fobar, M. Burger, P. J. Skrodzki, K. C. Hartig, A. T. Motta, and I. Jovanovic, *Spectrochim. Acta B*, 2018, **141**, 44-52. <https://doi.org/10.1016/j.sab.2018.01.003>
26. A. V. Smith and B. T. Do, *Appl. Opt.*, 2008, **47**, 4812-4832. <https://doi.org/10.1364/ao.47.004812>
27. Y. Qiu, J. Wu, H. Yu, I. B. Gornushkin, J. Li, Q. Wu, Z. Zhang, and X. Li, *Appl. Surf. Sci.*, 2020, **533**, 147497. <https://doi.org/10.1016/j.apsusc.2020.147497>